ACS APPLIED MATERIALS & INTERFACES

Research Article

Cite This: ACS Appl. Mater. Interfaces 2018, 10, 19948−19956

www.acsami.org

Spray-Coating Thin Films on Three-Dimensional Surfaces for a Semitransparent Capacitive-Touch Device

Tian Carey,[†] Chris Jones,[‡] Fred Le Moal,[‡] Davide Deganello,[§] and Felice Torrisi*[,†]

[†]Cambridge Graphene Centre, University of Cambridge, Cambridge CB3 0FA, U.K.

[‡]Novalia Ltd, Impington, Cambridge CB24 9N, U.K.

[§]Welsh Centre for Printing and Coating, College of Engineering, Swansea University, Swansea SA1 8EN, U.K.

Supporting Information

ABSTRACT: Here, we formulate low surface tension (~30 mN/m) and low boiling point (~79 °C) inks of graphene, single-wall carbon nanotubes and conductive polymer poly(3,4-ethylenedioxythiophene):poly(styrenesulfonate) (PEDOT:PSS) and demonstrate their viability for spray-coating of morphologically uniform ($S_q \approx 48 \pm 3$ nm), transparent conducting films (TCFs) at room temperature (~20 °C), which conform to three dimensional curved surfaces. Large area (~750 cm^2) hybrid PEDOT:PSS/graphene films achieved an optical transmission of 67% in the UV and 64% in the near-infrared wavelengths with a conductivity of ~10^4 S/m. Finally, we demonstrate the spray-coating of TCFs as an electrode on the inside of a poly(methyl methacrylate) sphere, enabling a semitransparent (around 360°) and spherical touch sensor for interactive devices.

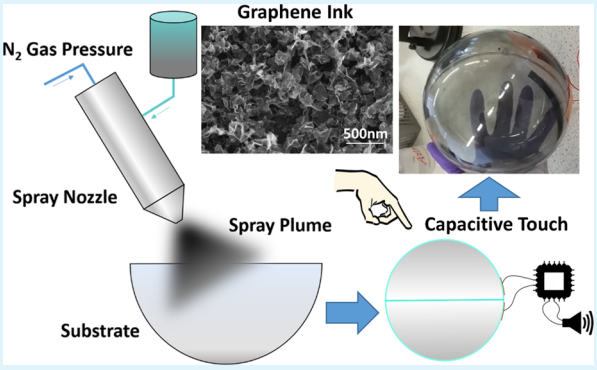

KEYWORDS: *spray coating, 3D surfaces, graphene, carbon nanotubes, transparent conducting film, capacitive touch sensor, liquid phase exfoliation*

INTRODUCTION

Electronics conformable to three-dimensional (3D) irregular surfaces is a rapidly emerging field with a huge potential impact in medical, communication, electronic, textile, and automotive industries, enabling the integration of circuits and devices on substrates with increased shape complexity.[1−3] Moreover, as electronics become more advanced and ubiquitous, there will be a need for smaller devices which maximize volume utilization and compactness in all three spatial dimensions.[2] Industry commonly uses techniques such as laser direct write[4] and two-component injection molding[5] to transfer metals via electroplating onto irregular surfaces. However, electroplating is often time-consuming, is limited to metals, and can create waste chemicals which are hazardous to the environment.[6] An alternative method of depositing materials (including metals, insulators, and semiconductors) on 3D surfaces is by solution processing, that is, in the form of an ink. Several techniques have been developed for printing of inks on 3D surfaces[7] and can generally be divided into three categories: filamentary-based (i.e. threadlike) techniques such as direct ink writing (robocasting);[8] stamping techniques such as pad printing;[9] and liquid-based techniques such as aerosol jet,[10] hydrographic printing,[11] and spray coating.[12] Additionally, some conventional ink-based techniques such as inkjet and screen printing,[12] which typically require a planar substrate, have been adapted for use on 3D surfaces by placing the substrate on a rotary system which allows the nozzle head or printing mesh to remain perpendicular to the target substrate. Thermoforming (in-mold electronics) can also be used in conjunction with techniques such as spray, inkjet, screen, flexo, and gravure[12] to deposit inks on flat planar polymer substrates, which are then made pliable by applying heat which can hot-form the polymer into a complex 3D shape.[13]

The use of several of these techniques has already been demonstrated to create novel devices. Reference 1 used direct ink writing of silver ink antennas on the surface of a hollow glass hemisphere.[1] Magnetometers, which included a microprocessor, LED, and magnetic Hall effect sensor, have also been connected with silver using laser direct write.[2] Reference 11 used hydrographic printing to transfer single layer graphene for use as a TCF in an electroluminescent wire for application in wearable electronics.[11] Reference 14 used printed silver ink on a polyethylene terephthalate (PET) bottle for radio-frequency identification antennas.[14] Humidity sensor-on-chip devices have been fabricated with silver ink deposited by aerosol jet,[15] while spray coating has also been used to deposit manganese dioxide/reduced graphene oxide composite onto a 3D nickel foam for super capacitive applications.[16]

Received: February 14, 2018
Accepted: May 10, 2018
Published: May 10, 2018

DOI: 10.1021/acsami.8b02784
ACS Appl. Mater. Interfaces 2018, 10, 19948−19956

The development of printable devices around 3D objects will require the deposition of different materials (e.g., metals, nanowires, organic polymers, carbon nanotubes, and graphene) most likely in hybrid arrangements depending on the desired electrical, optical or mechanical application of the final device. One of the most important and simple elements of many devices are transparent conducting films (TCFs) and could be used as an electrode material in applications such as curved smart windows on planes, which can control glare for pilots and passengers,[17] large displays, or photovoltaics to cover buildings,[17] or even for a sensor in wearable electronics,[3] where the device should be as unintrusive as possible and therefore must conform to the body.

Graphene, single-wall carbon nanotubes (SWNTs), poly(3,4-ethylenedioxythiophene) poly(styrenesulfonate) (PEDOT:PSS), and hybrid combinations of them have emerged as TCF materials in printed,[18] flexible,[19] and conformable electronics.[20] Typically, TCF performance is compared using a figure of merit (FOM).[20,21] A commonly used FOM is derived from a relationship between transmittance (T_{op}) and sheet resistance (R_s) defined by,[20,21]

$$T_{op} = \left[1 + \frac{Z_0}{2R_S}\frac{\sigma_{op}}{\sigma_{dc}}\right]^{-2} \quad (1)$$

where Z_0 is the impedance of free space (377 Ω), σ_{op} is the optical conductivity, and σ_{dc} is the bulk dc conductivity. The ratio σ_{dc}/σ_{op} is used as the FOM because high values imply films which have both high conductivity and transmittance. PEDOT:PSS (σ_{dc}/σ_{op} = 36)[22] can be dispersed in solvent readily; however, it has poor environmental stability (i.e., sheet resistance will increase as a function of time), has bad electrical homogeneity (i.e., variation in conductivity across films),[23,24] and absorbs light in the infrared region (~1200 nm).[25] Conversely, solution-processed graphene (σ_{dc}/σ_{op} = 0.01−15)[21] and SWNTs (σ_{dc}/σ_{op} = 10−100)[21] offer several advantages such as environmental stability,[26] flexibility,[3] sustainability,[27] and broadband wavelength T_{op}.[19,28]

Spray coating is highly suited to deposit these materials and create electronics on 3D surfaces as it is a large-area, high-throughput, inexpensive, and industrially scalable process[29] that can be used to create thin films of material which conform to the shape of the substrate. Moreover, spray coating is a contact-free technique suitable for any substrate material and is particularly appropriate when low temperature processing is necessary (e.g., deposition on plastics which deform between 100−200 °C).[30] In this work, we investigate the parameters influencing the spraying of PEDOT:PSS, SWNTs, graphene, and hybrid PEDOT:PSS/graphene inks and use them to demonstrate high-quality spray-coated TCFs on flexible and 3D substrates.

EXPERIMENTAL SECTION

Spray Coating Parameter Optimization. The atomization process involves liquid breakup because of the application of mechanical energy, which results in the production of a spray that contains a distribution of micron-size drops.[31] The liquid properties of liquid−vapor surface tension (γ_{lv}), viscosity (η), and density (ρ) control the deformation of the droplets[29] and hence atomization. Atomization takes place when the dynamic pressure of an external force (normally applied by a gas, such as nitrogen) exceeds the internal pressure of the liquid droplet. The ratio of the gas dynamic pressure ($v_{air}^2\rho_{air}$) to liquid capillary pressure (γ_{lv}/d_{liq}) represents the dimensionless Weber number (We) given by[29]

$$We = \frac{v_{air}^2 \rho_{air} d_{liq}}{\gamma_{lv}} \quad (2)$$

where v_{air} is the velocity of the air flow, ρ_{air} is the density of the air flow, and d_{liq} is the diameter of the droplet. The v_{air} is controlled by the atomization pressure (A_p) of the air-assisted atomizer (i.e., the gas pressure applied across the liquid ejected from the spray nozzle), which is set to A_p = 9 psi (the maximum allowed by our system) to ensure the atomization of each ink. The influence of viscosity on atomization can be represented by the ratio of an internal viscosity force to an interfacial surface tension force[31] known as the Ohnesorge number (Oh) defined as[32]

$$Oh = \frac{\eta}{\sqrt{\rho\gamma_{lv}d_{liq}}} \quad (3)$$

Atomization will only occur for values of We greater than a critical Weber number (We_{crit}), which depends on Oh (which is proportional to η) and also how v_{air} varies with time.[32] In an air-assist atomizer, liquid is exposed to a sudden increase in v_{air} with time and therefore We_{crit} > 13 as described in ref 34.[32] Consequently, all our inks were engineered to be above this threshold ($We > We_{crit}$) estimating v_{air} (>10 m/s)[29] and d_{liq} (~315 μm). Moreover, at Oh > 0.5 the liquid deformation will be hindered and will not be large enough to sufficiently atomize the liquid.[32] Therefore, for each ink, we use Oh < 0.2 to avoid η hindering the atomization process.[33] Once the droplets contact the substrate and overcome initial impact dynamics,[34] the droplets settle according to Young's equation which is defined as[35]

$$\gamma_{sv} = \gamma_{sl} + \gamma_{lv}\cos\theta \quad (4)$$

where γ_{sl} is the interfacial tension between the liquid and substrate and γ_{sv} is the surface energy of the substrate.[35] The nozzle speed (s), nozzle height (h) (distance from substrate), and flow rate (F_R) (i.e., rate of liquid ejection from the spray nozzle) are closely related as they control the amount of liquid deposited per unit area.[12] F_R is set to 12.5 mL/min to control the quantity of ink flowing out of the nozzle, while h and s are set to 8 cm and 12.7 cm/s, respectively, to control the location where the ink is deposited. The deposited material is then transported due to convectional flow (i.e., temperature-mediated particulate transport) during drying.[36] This effect is described by the coffee-ring effect, whereby the increased surface area at the edges (because of the curvature of a droplet) results in an increased evaporation rate. The lost liquid gets replenished by the liquid from the interior, which results in an outward flow that carries the dispersed material to the edge of the droplet.[36]

The subsequent deposition of the material from these droplets into morphologically uniform (i.e., a continuous layer of material) films has been considered a challenge[37,38] primarily because of the large number of parameters involved in the drying process. However, uniform thin film morphology is essential in many devices (e.g., solar cells,[38] OLEDs,[39] field-effect transistors,[26] saturable absorbers,[28] and TCFs[20,21]) to reduce defects, improve efficiency or field-effect mobility,[26] and achieve a percolating film.[18,40] The ink properties such as boiling point (B_p), η, and γ_{lv}[29] can affect morphological uniformity of these films. Increasing η can hinder the movement of particulates[41] and could likely improve the morphological uniformity of a sprayed film; however, increasing the η of an ink often requires the addition of a rheology modifier,[26] which significantly reduces the electrical, mechanical, and optical performance of a TCF. The γ_{lv} is an important parameter as it will affect how the droplets spread and coalesce on the substrate surface according to Young's equation, while T has been identified as a parameter which minimizes droplet coalescence.[42−44] Therefore, we will focus our study on three parameters T, γ_{lv}, and B_p to enhance or minimize the coffee-ring effect, which alters film uniformity.[42−44] Moreover, decreasing B_p will decrease the drying time of the TCFs, which is important for maximizing the throughput of the spray coating process. The interplay between T, B_p, and γ_{lv} is still unclear, while determining favorable values for B_p and γ_{lv} is desirable for the optimal production of spray-coating graphene, CNT, and polymer inks. Therefore, we explore

DOI: 10.1021/acsami.8b02784
ACS Appl. Mater. Interfaces 2018, 10, 19948−19956

Table 1. Breakdown of Each Ink Formulation Presented in This Work, in Addition to a Summary of Their Ink Properties, Including Surface Tension, Viscosity, Density, Boiling Point, and Ink Concentrations

ink no.	formulation	surface tension (mN/m)	viscosity (mPa s)	density (g/cm^3)	boiling point (°C)	particulate concentration (mg/mL)
ink 1	GNP-CMC-Triton-X-DiW	35	1.2	1.02	99	0.8
ink 2	GNP-CMC-DiW	74	1.3	1.01	100	0.12
ink 3	GNP-Eth	30	0.7	0.73	79	2.6
ink 4	SWNT-Eth	30	1.3	0.76	79	0.12
ink 5	GNP-Eth	31	1.2	0.77	79	0.12
ink 6	PEDOT:PSS:Eth	30	13	0.78	80	3.03
ink 7	Gr-PEDOT:PSS-Eth	31	0.81	0.79	77	0.094

these three parameters through ink formulation and investigation of film morphology.

Optimization of Inks for Film Uniformity. First, we investigate the effect of B_p and γ_{lv} on the uniformity of sprayed films. For simplicity, we investigate this effect on graphene-based inks. To do this, we engineer three different graphene nanoplatelet (GNP) inks (Table 1, ink 1−3) designed as follows; ink 1 (B_p = 99 °C, γ_{lv} = 35 mN/m), ink 2 (B_p = 100 °C, γ_{lv} = 74 mN/m), and ink 3 (B_p = 79 °C, γ_{lv} = 30 mN/m). All three inks had similar viscosities and densities of ∼1 mPa s and ∼1 g/cm^3, respectively (Table 1), but different B_p and γ_{lv}. GNP powder (GR1, Cambridge Nanosystems) was selected as it can be easily dispersed and requires minimal processing. The GNPs are produced by cracking methane gas in a plasma torch as previously reported[28] and have a peak lateral size and thickness of 1.04 μm and 4−5 nm, respectively.[28] The three inks were produced by ultrasonicating GNPs in carboxymethylcellulose sodium salt (CMC)/Triton-X-100/deionized water (DiW) (ink 1), CMC/DiW (ink 2), and ethanol (Eth, ink 3) for 1 h followed by centrifugation at 1k rpm for 20 min to remove thick flakes (see Methods for further details). After centrifugation, γ_{lv}, η, and B_p are measured using the pendent drop method (FTÅ1000B), a parallel plate rotational rheometer (Bohlin Instruments C-VDR), and a differential scanning calorimeter (Q20 DSC TA Instruments), respectively (see Methods) while optical absorption spectroscopy (OAS) (Agilent Cary 7000 UMS) is used to estimate the ink concentration of GNP[45,46] (Table 1, Supporting Information Figure S1−3).

Before attempting to spray around the three dimensions, we investigate the film uniformity after spraying inks on planar PET (Hififilm PMX729) substrates. Typically, PET has a low surface energy (γ_{sv} ≈ 50 mN/m) (calculated with the sessile drop technique, Supporting Information Figure S4) because of the lack of hydroxyl groups on the polymer chains,[30] which according to Young's equation if sprayed on would likely result in the formation of several unconnected islands of droplets and consequently in a non-percolating network. To obviate this effect, we perform a UV ozone (Nano Bio Analytics UVC-1014) treatment for 15 min (4 W at 254 nm), which increases γ_{sv} to ∼69 mN/m (Supporting Information Figure S4a). Then, the impact T has on uniformity of the coating is investigated by spray-coating ink 1, 2, and 3 in a single pass (i.e., the spray nozzle is brought across the substrate perpendicularly once) through the aperture (2.5 cm^2) of an aluminum mask and onto the PET substrates at h = 8 cm, s = 12.7 cm/s, A_p = 9 psi, and F_R = 12.5 mL/min at different T from 20 to 70 °C. Upon deposition of these inks, Marangoni flow (also known as the Marangoni effect) can sometimes be induced as a consequence of γ_{lv} gradients.[47] Consequently, liquid (and thus GNPs) moves from regions of lower γ_{lv} to higher γ_{lv}. The γ_{lv} depends on both T and chemical composition; therefore, Marangoni flow can be induced by gradients in either T or chemical concentration (in our case, our GNPs, polymers, or surfactants) at the wet film interface.[47] We make two assumptions here: first, because our films are large (2.5 cm) the evaporation rate across the film is constant, and thus, the T gradient is negligible, and second, our polymer (i.e., CMC) and surfactant (TritonX-100) are stabilizing the GNPs and are not residing on the surface of the wet film, and therefore, the polymer/surfactant gradient is minimal; hence, the effect of the Marangoni flow can be neglected for our inks. The addition of GNP to an ethanol solution (ink 3) does not appear to significantly change the ink properties from pure ethanol, likely because of the low volume fraction of GNP (<0.3%, assuming a graphene density of 0.72 g/cm^3).[28]

We use a simple desktop scanner (HP Deskjet 3050A) to acquire optical images of our deposited films resulting from the deposition of inks 1−3 (see Supporting Information Figure S5−S7). Optical scanning operates by shining light on the film and collecting the reflected light in a CCD camera (see Methods and Supporting Information section 1.3 for more details and discussion). Figure 1 shows optical scans of the sprayed films for inks 1−3 at 20, 40, and 70 °C respectively. We use these to obtain a visual indication of morphological uniformity (over a 2.5 cm by 2.5 cm area) of the sprayed films. Figure 1, row a, shows the sprayed films of ink 1 (B_p = 99 °C, γ_{lv} = 35 mN/m). In this case, the droplets have sufficient time to coalesce (i.e., come together to form one large liquid film) before drying because of the high boiling point (∼99 °C). Once the liquid film dries, a single large coffee ring is formed, which becomes more defined with increasing T. An optical profiling system (Wyko NT9300) is used to quantify the root mean squared height roughness (S_q) of the films. The changing morphology can be quantified by S_q increasing from 78 ± 24 nm at 20 °C to 136 ± 14 at 70 °C (see Supporting Information Figure S8a), which indicates that the film becomes less morphologically uniform with increasing convectional flow (i.e., temperature) because of the greater amount of material that is deposited around the edge of the film.[36]

Figure 1, row b, shows the scanned films of ink 2 (B_p = 100 °C, γ_{lv} = 74 mN/m). Despite the surface treatment increasing the surface energy of the PET (γ_{sv} ≈69 mN/m), isolated coffee rings were still observed, which can only be explained by the higher surface tension

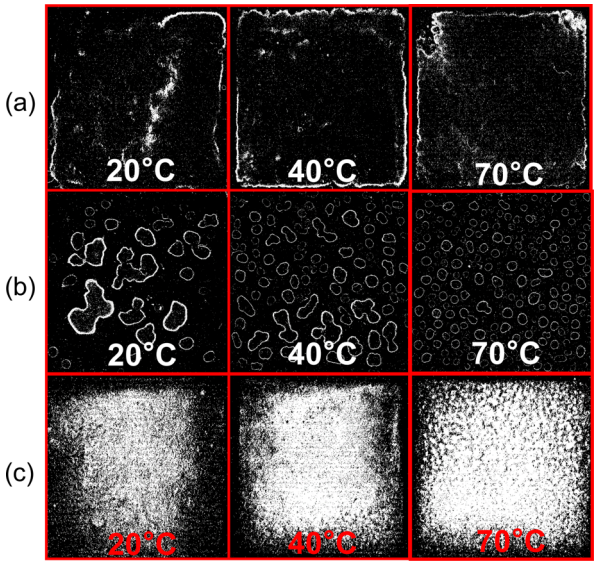

Figure 1. (a) Morphology of (row a) ink 1 (B_p = 99 °C, γ_{lv} = 35 mN/m), (row b) ink 2 (B_p = 100 °C, γ_{lv} = 74 mN/m), and (row c) ink 3 (B_p = 79 °C, γ_{lv} = 30 mN/m) as a function of temperature. Each box is 2.5 cm by 2.5 cm in length and width.

DOI: 10.1021/acsami.8b02784
ACS Appl. Mater. Interfaces 2018, 10, 19948−19956

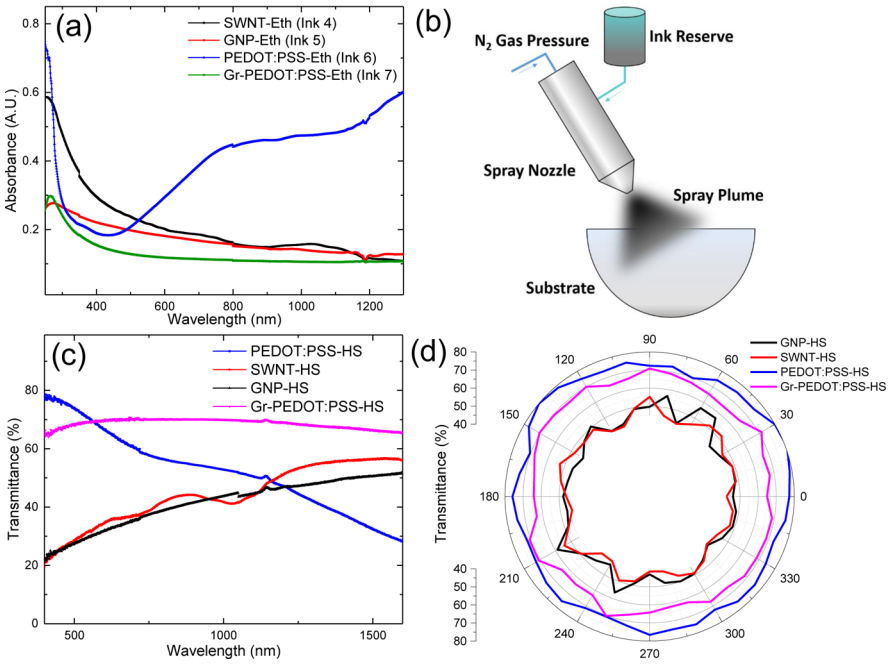

Figure 2. (a) Absorption spectra for ink 4–7 from visible to n-IR wavelengths. (b) Schematic of the spray coating process with an air-assist spray nozzle being used to spray graphene ink around a 3D PMMA hemisphere. (c) Film transmittance as a function of wavelength and (d) angular film transmittance (550 nm) characterized using OAS.

($\gamma_{lv} \approx 74$ mN/m) of ink 2. Here, several isolated droplets are formed immediately after the spray reaches the substrate because of coalescence of the droplets. The coalesced droplets then dry and create several isolated coffee rings seen as the white distorted circles, which create a surface with an extremely varied surface roughness ranging from $S_q \approx 20$ nm in uncoated areas at the center or outside of coffee rings to $S_q \approx 260$ nm on the coffee ring edges which remains consistent with increasing temperature (see Supporting Information Figure S8a). By increasing the substrate temperature, the droplets dry faster, which hinders coalescence and thus the number of droplets (N) per unit area (cm^2) increases from ~5 N/cm^2 at 20 °C to ~22 N/cm^2 at 70 °C (Supporting Information Figure S8b). Moreover, the decreased droplet coalescence is also verified by a decrease in the average Feret's diameter (i.e., a measure of an object size along a specified direction) from 3.8 to 1.3 mm (Supporting Information Figure S8c).

Figure 1, row c, shows the scanned films of ink 3 (B_p = 79 °C, γ_{lv} = 30 mN/m). In this case, the presence of a coffee ring is minimized by the decreased B_p (79 °C) of ink 3 with respect to inks 1 and 2. It is likely that ink 3 evaporates faster than ink 1 and 2 because of its B_p, and thus, the transport of graphene into a coffee ring is reduced.[26,28] As T increases, the average S_q increases from 48 ± 3 nm at 20 °C to 101 ± 13 nm at 70 °C (Supporting Information Figure S8a). This is likely due to the Leidenfrost effect which forms a thin vapor layer at the liquid–substrate interface because of the rapid evaporation of solvent.[48] The vapor film can transport material away from the point of deposition, which becomes more prominent with increasing T due to the increased evaporation rate of the solvent. Therefore, lower T (20 °C) should be used to minimize this effect and create a smoother and more uniform film.

Spray-Coating of TCFs. Following the previous experiments, the most morphologically uniform films can be created when the parameters T, γ_{lv}, and B_p are minimized obtaining S_q as low as 48 ± 3 nm for a single spray pass. We achieved this by spraying ink 3 at $T \approx$ 20 °C. Here, the ethanol ensures a γ_{lv} of 30 mN/m and a B_p of 79 °C. With this knowledge, we formulate SWNT (SWNT-Eth, ink 4), GNP (GNP-Eth, ink 5), PEDOT:PSS (PEDOT:PSS-Eth, ink 6) inks and a hybrid graphene/PEDOT:PSS (Gr-PEDOT:PSS-Eth, ink 7) ink (~1 v/v % PEDOT:PSS, see Methods for further details), matching these parameters to spray-coat a uniform TCF on a curved poly(methyl methacrylate) (PMMA) hemisphere. We selected SWNTs, GNPs, and PEDOT:PSS to ensure that the ink formulation and subsequent spray-coating of morphologically uniform films is adaptable to several material archetypes, while a hybrid ink is produced to take advantage of PEDOT:PSS's high conductivity and graphene's environmental sustainability, affordability, and low percolation threshold. The γ_{lv}, η, and B_p are characterized as before and presented in Table 1. OAS is used to estimate the GNP and SWNT concentration in the inks at (λ = 660 nm) via the Beer–Lambert law according to the relation $A = \alpha cl$, where A is the absorbance, l [m] is the light path length through the cuvette, c [g/L] is the concentration of dispersed graphitic material, and α [L/g^1 m] is the absorption coefficient. Figure 2a shows the absorption spectra of ink 4 (black curve), ink 5 (red curve), ink 6 (blue curve), and ink 7 (green curve) resulting in concentrations of ~0.12, ~0.12, ~3.03, and ~0.094 mg/mL for SWNT-Eth, GNP-Eth, PEDOT:PSS-Eth, and Gr-PEDOT:PSS-Eth inks, respectively. We used $\alpha \approx 3264$ mL/mg m[49] for SWNT-Eth, $\alpha \approx 2460$ mL/mg m[46] for GNP-Eth, and $\alpha \approx 231$ mL/mg m for PEDOT:PSS-Eth (Supporting Information Figure S1b). We approximate $\alpha \approx 2460$ mL/mg m for Gr-PEDOT:PSS-Eth because of the negligible amount of PEDOT:PSS used compared to GNPs. It is worth noting that PEDOT:PSS-Eth needed to be formulated at a significantly higher c (3.03 mg/mL) compared to the other GNP, SWNT, and Gr-PEDOT:PSS-Eth inks, as conductive percolating films could not be produced at a c of 0.12 mg/mL. This shows the advantage of using a material such as graphene with a large lateral size (117 nm, Supporting Information section 1.1), as it can create a percolating network with a high conductivity (1×10^4 S/m) at a low concentration (~0.1 mg/mL).

Before we construct a transparent capacitive touch device on a spherical surface, we first spray films of each ink (using a SCS Precisioncoat V) on two hemispheres and investigated their performance as a curved TCFs. A PMMA hemisphere (diameter 15.5 cm) was positioned under the spray nozzle as shown in the image of Figure 2b, and the inks are sprayed around 360° (25 layers to ensure we reach the bulk regime) at nozzle tilt angles of 45, 38, 30, 24, 15, and 9° at h = 6 cm, s = 12.7 cm/s, F_R = 7 mL/min, and A_p = 9 psi to control the amount of ink deposited per unit area. This process, under the same conditions, was undertaken for each ink (from 4 to 7) individually, for a total of 25 spray passes to create hemispherical (HS) TCFs of ink 4 (SWNT-HS), ink 5 (GNP-HS), ink 6 (PEDOT:PSS-

DOI: 10.1021/acsami.8b02784
ACS Appl. Mater. Interfaces 2018, 10, 19948–19956

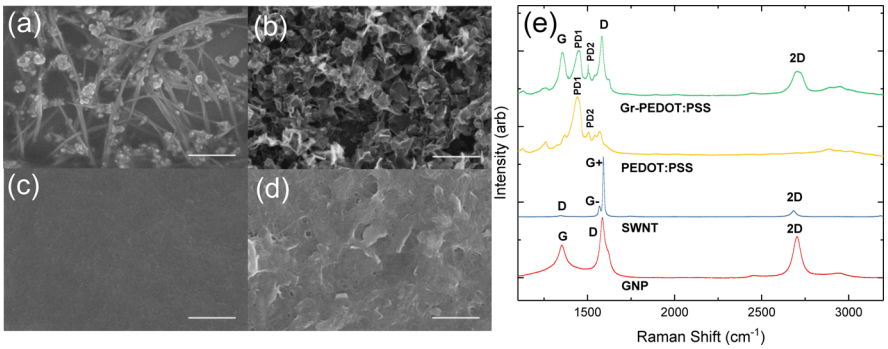

Figure 3. SEM images of (a) SWNTs (ink 4), (b) GNP (ink 5), (c) PEDOT:PSS (ink 6), and (d) Gr-PEDOT:PSS (ink 7), where the scale bar in each case corresponds to 500 nm. (e) Raman spectra acquired at 514.5 nm on the spray-coated films of SWNTs (blue), PEDOT:PSS (yellow), GNPs (red), and Gr-PEDOT:PSS (green).

HS), and ink 7 (Gr-PEDOT:PSS-HS). We notice that even though we have changed the substrate to a more hydrophobic material than our treated PET (PMMA, $\gamma_{sv} \approx 41$ mN/m), there is no noticeable change in the morphological uniformity, requiring no further UV-ozone surface treatment to further increase γ_{sv}. Moreover, each layer only takes about 10 s to spray and 50 s to dry, demonstrating the high throughput nature of the spray coating process.

The T_{op} of the resulting spray-coated hemispheres were then characterized using OAS. Figure 2c plots the film transmittance as a function of wavelength for the SWNT-HS, GNP-HS, PEDOT:PSS-HS, and Gr-PEDOT:PSS-HS films. PEDOT:PSS-HS (blue curve) showed the highest transmittance (70%) at 550 nm decaying quickly to lowest transmission (16%) in n-IR (2100 nm) because of free carrier absorption.[50] Conversely, the SWNT-HS (red curve) and GNP-HS (black curve) films had much higher transmittance in the infrared of 59 and 58% at 2100 nm and lower transmission of 32 and 30% at 550 nm, respectively. Unlike the GNPs, the SWNT spectrum shows two transmission dips at 729 and 1033 nm indicative of the SWNT optical resonances of the metallic and semiconducting nanotubes, respectively.[51] The Gr-PEDOT:PSS-HS film offers both a high transmission in the visible (67% at 550 nm) and in n-IR (63% at 2100 nm), while avoiding the SWNT resonance peaks. Moreover, the SWNT-HS and GNP-HS retain these transmittances (standard deviation ± 4%) along with the PEDOT:PSS-HS and Gr-PEDOT:PSS-HS (standard deviation ± 3%) over 360° as shown in Figure 2d. It is important to note that the transmission of PEDOT:PSS-HS drops to roughly half the value of GNP-HS and SWNT-HS past 1200 nm wavelength. The almost constant optical transmittance of the Gr-PEDOT:PSS film together with the higher optical transmittance over SWNTs and graphene and hybrid opens up to a broad range of applications of such large-area sprayed films in infrared or terahertz devices, for communications and energy such as in solar cells[52] or n-IR LEDs.[53]

The characterization of large-area (~750 cm^2) curved 3D substrates such as our HS TCFs under atomic force microscopy (AFM), scanning electron microscopy (SEM), and Raman spectroscopy is not feasible because of their curved geometry. To further characterize our sprayed films and determine the material quality via Raman spectroscopy, qualitative morphology SEM and film thickness AFM, we replicate the same films on a flat Si/SiO_2 ($\gamma_{sv} \approx 56$ mN/m) substrate using inks 4−7 and the same spraying parameters which were used to spray-coat the hemispheres. AFM (Bruker Dimension Icon) is used to determine the average thickness (t) of the PEDOT:PSS ($t \approx 359$ nm), SWNT ($t \approx 231$ nm), GNP ($t \approx 290$ nm), and Gr-PEDOT:PSS ($t \approx 156$ nm) films (Supporting Information Figure S9). Consequently, the conductivity (σ) can be estimated using $\sigma^{-1} = R_s t$ (R_s values reported in Supporting Information section 1.4). We find that the PEDOT:PSS and the Gr-PEDOT:PSS film showed the highest σ (4.7×10^4 and $\sim 1 \times 10^4$ S/m, respectively) amongst all the films, whereas SWNT and GNP films had a substantially lower conductivity (~94 and ~3 S/m, respectively). The electrical transport mechanism in each film is limited by Mott's law for variable range hopping $\sigma(T) = \sigma_0 \exp[-(T_0/T)^{1/(1+n)}]$, where n depends on the dimensionality of the system.[54] Figure 3a−d presents the SEM images of each film (see Methods). Figure 3a shows the SEM image with a typical interwoven arrangement of SWNTs on the substrate. The SWNT bundles can be seen to be a few μm in length, while it is likely that the residual particles adhering to the side of the SWNTs may be attributed to residuals of the Triton-X surfactant. In Figure 3b, the SEM image shows a network of percolated overlapping GNP flakes which appear to be slightly crumpled, whereas the SEM image in Figure 3c shows the smooth morphology of the PEDOT:PSS film. Finally, Figure 3d shows an SEM image of the Gr-PEDOT:PSS film that consists of a combination of the pristine graphene and PEDOT:PSS. The graphene flakes can be seen embedded in the PEDOT:PSS matrix and protruding outward at various points throughout the film. The pristine graphene flakes appear to be more rigid than the GNP likely because of their thickness (~6 nm), which is ~2 nm greater than the GNPs (Supporting Information section 1.1).

Figure 3e plots the Raman spectra (taken at 514 nm) of the spray-coated films. These are used to assess the quality of the films on Si/SiO_2 (see Methods). The red and green curves present a G peak at ~1580 cm^{-1} which corresponds to the E_{2g} phonon at the Brillouin zone center,[55] while the D peak is due to the breathing modes of sp^2 rings and requires a defect for its activation by double resonance.[55,56] The 2D peak (red and green curves) is the second order of the D peak and can be always seen, even when no D peak is present, because the activation of two phonons with the same momentum, one back-scattering from the other, does not require defects and irregular edges.[56] A single Lorentzian fit of the 2D peak indicates that the graphene comprises electronically decoupled graphene layers. The analysis of the G peak dispersion (Disp(G), more details in Methods) allows one to discriminate between disorder localized at the edges or in the bulk of the samples.[57,58] In the case of the Gr-PEDOT:PSS (green curve) (Disp(G) ≈ 0.03 cm^{-1} nm^{-1}) and GNP (red curve) (Disp(G) ≈ 0.09 cm^{-1} nm^{-1}), the Disp(G) is lower than what expected for disordered carbon.[57] Moreover, we can conclude that the D peak intensity is mostly attributed to the edges of the sub-micrometer flakes, rather than to a large amount of structural defects within the flake.[59] The SWNT spectra (blue curve) shows a G^+ peak at 1590 cm^{-1} and a G^- peak at 1568 cm^{-1}. The G^+ peak is induced by carbon atom vibrations along the nanotube axis (longitudinal optic mode), whereas the G^- peak relates to the vibration of carbon atoms along the circumference of the CNT (transverse optic phonon). The intensity and line shape depend on the metallic or semiconducting nature of the CNTs under investigation.[60] A low intensity Lorentzian G^- peak indicates that the CNT film is populated with mostly semiconducting CNTs.[60] The D peak located at 1350 cm^{-1} is related to the defects of the SWNTs. The ratio of I_D/I_G^+ (~0.02) is indicative that the sample is highly crystalline and has a low defect content. The PEDOT:PSS spectra (yellow curve) exhibit several peaks, which are typically assigned to PEDOT:PSS's carbon stretching vibrations.[61,62] The two most dominant peaks are found at ~1440 cm^{-1} (PD1) and ~1505 cm^{-1} (PD2) with stronger intensity and are assigned to the

DOI: 10.1021/acsami.8b02784
ACS Appl. Mater. Interfaces 2018, 10, 19948−19956

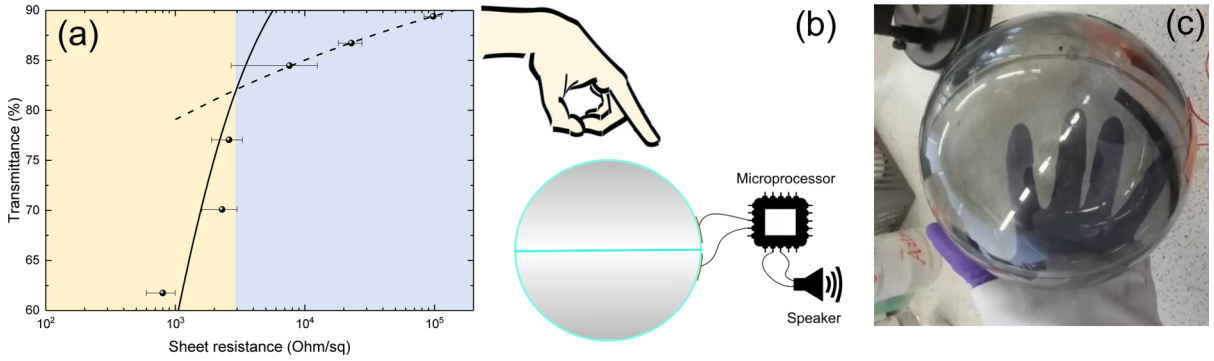

Figure 4. (a) Optical transmittance as a function of the sheet resistance, where the bulk regime is shown in yellow and the percolation regime shown in blue. Error was calculated by standard deviation of mean. (b) Gr-PEDOT:PSS-Eth ink is sprayed around two PMMA hemispheres, which are then joined to form a sphere. The conductive sphere is then connected to a microprocessor, which results in sound when touched. (c) Photo of the spray-coated semi-transparent capacitive-touch device.

asymmetric $C_\alpha = C_\beta$ stretching and symmetric $C_\alpha = C_\beta$ (−O) stretching vibrations, respectively.[61,62] In the Gr-PEDOT:PSS spectra (green curve), the PD1 and PD2 peaks are also found in conjunction with the G, D, and 2D peaks, indicating the presence of both PEDOT:PSS and graphene.

Semitransparent Capacitive Touch Device. Touch-sensitive devices on 3D surfaces using several technologies have been already developed including resistive, piezoelectric, optical, triboelectric, and capacitive-touch sensors;[63] however, one of the most predominant applications is capacitive-touch.[64] The TCFs we have developed can be used as transparent curved electrodes in a capacitive-touch device. The Gr-PEDOT:PSS-HS is ideal for this application as it has high conductivity (~1×10^4 S/m), which easily matches the requirement for touch panels,[65] while it also offers sufficient T_{op} across the electromagnetic spectrum ~65% from 550 to 2100 nm. The performance of Gr-PEDOT:PSS-HS as a TCF is investigated by measuring R_s and T_{op} for thin films with various spray passes (25, 20, 15, 10, 5, and 4 passes) on PET ($\gamma_{sv} \approx 69$ mN/m) at the same spray parameters described previously. In Figure 4a, we show that R_s versus T_{op} follows eq 1 for a film in the bulk regime (yellow regime, i.e., a film where the dc conductivity is invariant with sample thickness), until it reaches the percolative regime (blue regime, i.e., the point at which the conductivity becomes dependent on the film thickness) at between 10 and 15 spray passes.[21] We also find $\sigma_{dc}/\sigma_{op} \approx 0.6 \pm 0.1$ using eq 1 for Gr-PEDOT:PSS-HS. This is in line with solution-processed graphene TCFs which have a $\sigma_{dc}/\sigma_{op} \approx 0.01-15$,[21] indicating that our film is comparable to state-of-the-art graphene TCFs.

A capacitive-touch panel consists of two conducting electrodes separated by a dielectric. As shown in Figure 4b, we combine two Gr-PEDOT:PSS-HS hemispheres, spray-coated with 25 layers of Gr-PEDOT:PSS-Eth to ensure that our film has reached the bulk regime. The Gr-PEDOT:PSS makes up the inner electrode while we use copper tape (~20 cm^2) to create a conductive electrode on the outside of the PMMA sphere ($t \approx 2.48$ mm) which is being used as the dielectric. The microprocessor (GPCE2P064A 16-bit Sound Controller) continuously charges and discharges (~30 μs) the copper tape through a 512 kΩ resistor. When in a charged state, a voltage (~3.3 V) is applied across the electrodes and an electric field is generated (~1.3 kV/m) which extends into the surrounding environment. When a user's finger is brought toward the electric field, a perturbation of the electric field is created[66,67] because the fingers increased permittivity ($\varepsilon \approx 40$)[68] over that of the air ($\varepsilon \approx 1$) that is displaced. The perturbation of the electric field creates an increase in capacitance,[66,67] which is detected by the microprocessor as an increase in the discharge time (~40 μs). A sound from a speaker (tectonic elements) is then made when an increase in discharge time is detected by the microprocessor. This application demonstrates how a spray-coated Gr-PEDOT:PSS TCFs, deposited over large area (~750 cm^2), at high throughput and low temperature (<100 °C), can be used as conformal transparent electrodes on curved 3D objects, which are cost-effective, up-scalable, and environmentally sustainable.

CONCLUSIONS

In this work, we demonstrate large-area (~750 cm^2) graphene, SWNT, and graphene/PEDOT:PSS TCFs deposited by spray-coating on 3D curved surfaces (such as a plastic sphere), operating over a large wavelength range (400−1600 nm) with an optical transmission of ~65% and film conductivity ~ 10^4 S/m. The low aerial roughness of ~48 ± 3 nm achieved over the entire sprayed surface area of the sprayed TCFs can be controlled by minimizing the surface tension (~30 mN/m), boiling point (~79 °C), and processing temperature (~20 °C). Finally, we demonstrate the viability of spray-coated graphene/PEDOT:PSS TCFs to act as conformal transparent electrodes on plastic hemispheres, enabling spherical transparent capacitive-touch devices.

METHODS

Ink Preparation for Uniformity Study. The inks were created as follows. GNPs (GR1, Cambridge Nanosystems) (5 mg/mL) were dispersed in deionized water with Triton-X-100 (Sigma-Aldrich; 1 mg/mL; used to decrease γ_{lv} to 35 mN/m) and carboxymethylcellulose sodium salt (average molecular weight MW = 700 000; Aldrich no. 419338; 0.1 mg/mL; used to minimize GNP aggregation in DiW) (dispersion 1). GNPs (5 mg/mL) were dispersed in DiW with just CMC (0.1 mg/mL) (dispersion 2). Finally, GNPs (5 mg/mL) were dispersed in ethanol (because of its intrinsic low $\gamma_{lv} \approx 30$ mN/m and $B_p \approx 79$ °C) (dispersion 3). All three dispersions were bath-sonicated (Fisherbrand FB13069) for 1 h to disperse the GNPs. The dispersions were then ultracentrifuged (Beckman Coulter Proteomelab XL-A) at 1k rpm for 20 min. Subsequently, the supernatant of the dispersions (i.e., the top 70%) was collected and labeled as GNP-CMC-Triton-X-DiW (ink 1), GNP-CMC-DiW (ink 2), and GNP-Eth (ink 3), respectively.

Ink Preparation for TCF Study. We formulated four inks (ink 4−7) as follows. SWNT-Eth ink (ink 4): SWNTs (Carbon Solutions, Inc P2-SWNT) were mixed in ethanol along with Triton X-100 (Sigma-Aldrich; 1 mg/mL) (dispersion 4). GNP-Eth ink (ink 5): GNPs (0.12 mg/mL; GR1, Cambridge Nanosystems) were dispersed in ethanol (dispersion 5). PEDOT:PSS-Eth ink (ink 6): PEDOT:PSS (25 v/v %; Sigma-Aldrich 739 316, 0.8 w/v in H_2O) was mixed in ethanol (dispersion 6). Gr-PEDOT:PSS-Eth ink (ink 7): graphite flakes (3 mg/mL; Sigma-Aldrich) and PEDOT:PSS (1 v/v %, i.e., 0.08 mg/mL; Sigma-Aldrich 739 316, 0.8 w/v in H_2O) in ethanol (dispersion 7). In the case of Gr-PEDOT:PSS-Eth, the PEDOT:PSS helps to disperse and stabilize the graphene without having to use nonconductive surfactants which act as a barrier to conductivity. The stabilization

DOI: 10.1021/acsami.8b02784
ACS Appl. Mater. Interfaces 2018, 10, 19948−19956

mechanism is first due to the $\pi-\pi$ interaction between the graphene sheets and the backbone of the PEDOT and second the electrostatic repulsion between the negatively charged PSS.[69] Dispersions 5 and 6 were bath-sonicated (Fisherbrand FB13069) for 1 h to create inks 5 and 6. Dispersion 4 was bath-sonicated for 4 h and was then ultracentrifuged (Beckman Coulter Proteomelab XL-A) at 5k rpm for 1 h while dispersion 7 was bath-sonicated for 9 h and was then centrifuged at 5k rpm for 1 h. Subsequently, the supernatant (i.e., the top 70%) was collected to create ink 4 and ink 7, respectively. The graphene flakes prepared by Gr-PEDOT:PSS-Eth have a peak lateral size and thickness of 117 and 6 nm, respectively (Supporting Information section 1.1).

Surface Tension and Surface Energy. The surface tension was measured using the pendent drop method (First Ten Angstroms FTA1000B). The shape of the drop results from the relationship between γ_{lv} and gravity. The γ_{lv} was then calculated from the shadow image of a pendant drop using drop shape analysis. The contact angle was also measured using this system by dispensing 1 μL of DiW onto PET and measuring the angle (θ_c) at which the water interface meets the solid surface. Knowing the contact angle and surface tension of water, the surface energy can be determined using Neumann's equation of state[35] (see Supporting Information section 1.2).

Rheology. A parallel plate rotational rheometer (DHR rheometer, TA instruments) was used to evaluate the viscosity of the inks as a function of shear rate. Shear thinning was observed in all inks, and the infinite-rate viscosity was found.

Density Measurement. The density of the inks was found by dispensing 1 mL of ink and measuring the corresponding weight using a microbalance (Sartorius).

Spray Coater Heater. The substrates were heated using a Kapton-based heater coupled to a proportional–integral–derivative controller (Omega CNi3233) to maintain the set temperature.

Differential Scanning Calorimetry. Phase transitions from the liquid to the gaseous phase were quantified using a Q20 DSC (TA instruments). First, ~10 mg of ink was added to a pan which was then sealed with a hermetic pinhole lid (diameter 75 μm). Thermal profiles are taken from an initial temperature of 25 °C which was then ramped at a rate of 5 °C/min to 200 °C. For each ink, a line of best fit can be extruded from the baseline and at the endothermic phase transition so that the boiling point for each ink can be determined.

Optical Scanning. The morphology of the spray-coated films on PET was investigated by utilizing a simple desktop scanner (HP Deskjet 3050A). White paper was placed behind the PET to provide a clear contrast difference between the deposited black graphene. The resolution of each scan was set to 2400 dots/inch. Images are collected in TIFF format to avoid data compression losses. Images which imply the uniformity of the spray-coated films can then be extracted by image analysis tools (ImageJ). The images are first transformed into 8-bit grayscale images so that each pixel was assigned a number between 0 and 255 defined by sum of the red, green, and blue parts of each pixel. The image was then inverted, where we assign pure black to have a pixel value of 0 and white a pixel value of 255. To segment the grayscale image into features of interest and filter-out the background noise, a threshold was applied to the image. All pixels with a grayscale value range from 0–246 are set as white (and considered the deposited material), while pixels with values greater than this can be considered to have a negligible coating and are therefore considered as noise and set to black.

Optical Profiling. The surface roughness of the spray-coated PET films was investigated using a Wyko NT9300 optical profiling system. An objective lens of ×44 magnification was used with a sampling distance of 240.88 nm. For each film, five spot measurements (115 × 154 μm) were obtained at evenly spaced intervals across the sample to obtain an average S_q.

Scanning Eelectron Microscopy. SEM images were taken with a high-resolution Magellan 400L SEM system. The field emission gun was operated at an accelerating voltage of 5 keV and a gun current of 6.3 pA. Images were obtained in secondary electron detection mode using an immersion lens and a TLD detector.

Raman Spectroscopy. The spray-coated graphene films on a Si/SiO_2 wafer were examined by Raman measurements, collected with a Reinshaw 1000 InVia micro-Raman spectrometer at 514.5 nm and a ×50 objective, with an incident power of ~0.1 mW. The G peak dispersion is defined as $\mathrm{Disp(G)} = \Delta\mathrm{Pos(G)}/\Delta\lambda_L$, where λ_L is the laser excitation wavelength.

■ ASSOCIATED CONTENT

Supporting Information

The Supporting Information is available free of charge on the ACS Publications website at DOI: 10.1021/acsami.8b02784.

OAS of inks 1, 2, and 3, additional characterization of inks, surface energy calculation for substrates, review of characterization techniques for thin films, and AFM and sheet resistance of TCF films (PDF)

■ AUTHOR INFORMATION

Corresponding Author

*E-mail: ft242@cam.ac.uk.

ORCID

Felice Torrisi: 0000-0002-6144-2916

Author Contributions

T.C. and F.T. conceived and designed the experiments. T.C. developed the inks, sprayed TCFs, and undertook UV–vis, AFM, SEM, Raman spectroscopy, optical scanning, DSC, rheometry, surface tension, and contact angle measurements. C. J. conceived and F.L.M. built the capacitive touch device. T.C. and F.T. analyzed the experimental data and discussed the results. T.C. and D.D. undertook WLI optical profiling measurements and discussed analysis and interpretation. The manuscript was written by T.C. and F.T. in close consultation with other authors.

Notes

The authors declare no competing financial interest.

■ ACKNOWLEDGMENTS

We acknowledge funding from ERC grant Hetero2D, the EPSRC grants EP/P02534X/1 and EP/M008827/1, the Royal Academy of Engineering Enterprise Scheme, the Trinity College, Cambridge, and the Isaac Newton Trust.

■ REFERENCES

(1) Adams, J. J.; Duoss, E. B.; Malkowski, T. F.; Motala, M. J.; Ahn, B. Y.; Nuzzo, R. G.; Bernhard, J. T.; Lewis, J. A. Conformal Printing of Electrically Small Antennas on Three-Dimensional Surfaces. *Adv. Mater.* **2011**, *23*, 1335–1340.

(2) Espalin, D.; Muse, D. W.; MacDonald, E.; Wicker, R. B. 3D Printing Multifunctionality: Structures with Electronics. *Int. J. Adv. Manuf. Technol.* **2014**, *72*, 963–978.

(3) Ren, J.; Wang, C.; Zhang, X.; Carey, T.; Chen, K.; Yin, Y.; Torrisi, F. Environmentally-Friendly Conductive Cotton Fabric as Flexible Strain Sensor Based on Hot Press Reduced Graphene Oxide. *Carbon* **2017**, *111*, 622–630.

(4) Islam, A.; Hansen, H. N.; Tang, P. T.; Sun, J. Process Chains for the Manufacturing of Molded Interconnect Devices. *Int. J. Adv. Manuf. Technol.* **2009**, *42*, 831–841.

(5) Chen, J. Y.; Young, W. B. Two-Component Injection Molding of Molded Interconnect Devices. *Adv. Mater. Res.* **2013**, *628*, 78–82.

(6) Agrawal, A.; Sahu, K. K. An Overview of the Recovery of Acid from Spent Acidic Solutions from Steel and Electroplating Industries. *J. Hazard. Mater.* **2009**, *171*, 61–75.

(7) Lewis, J. A.; Smay, J. E.; Stuecker, J.; Cesarano, J. Direct Ink Writing of Three-Dimensional Ceramic Structures. *J. Am. Ceram. Soc.* **2006**, *89*, 3599–3609.

DOI: 10.1021/acsami.8b02784
ACS Appl. Mater. Interfaces 2018, 10, 19948–19956

(8) Román-Manso, B.; Figueiredo, F. M.; Achiaga, B.; Barea, R.; Pérez-Coll, D.; Morelos-Gómez, A.; Terrones, M.; Osendi, M. I.; Belmonte, M.; Miranzo, P. Electrically Functional 3D-Architectured graphene/SiC Composites. *Carbon* **2016**, *100*, 318−328.
(9) Xiong, Y.; Qu, Z. Antenna 3D Pad Printing Solution Evaluation. *IEEE Antennas and Propagation Society, AP-S International Symposium (Digest)*; 2011, pp 2773−2776.
(10) Jabari, E.; Toyserkani, E. Micro-Scale Aerosol-Jet Printing of Graphene Interconnects. *Carbon* **2015**, *91*, 321−329.
(11) Zhang, Y.; Gui, Y.; Meng, F.; Li, L.; Gao, C.; Zhu, H.; Hao, Y. Graphene Water Transfer Printing for 3D Surface. *Proceedings of the IEEE International Conference on Micro Electro Mechanical Systems (MEMS)*; 2016, pp 13−16.
(12) Krebs, F. C. Fabrication and Processing of Polymer Solar Cells: A Review of Printing and Coating Techniques. *Sol. Energy Mater. Sol. Cells* **2009**, *93*, 394−412.
(13) Vanfleteren, J.; Bossuyt, F.; Plovie, B. A New Technology for Rigid 3D Free-Form Electronics Based on the Thermoplastic Deformation of Flat Standard PCB Type Circuits. *12th International Congress Molded Interconnect Devices*; 2016, pp 3−6.
(14) Merilampi, S. L.; Björninen, T.; Ukkonen, L.; Ruuskanen, P.; Sydänheimo, L. Characterization of UHF RFID Tags Fabricated Directly on Convex Surfaces by Pad Printing. *Int. J. Adv. Manuf. Technol.* **2011**, *53*, 577−591.
(15) Clifford, B.; Beynon, D.; Phillips, C.; Deganello, D. Printed-Sensor-on-Chip Devices − Aerosol Jet Deposition of Thin Film Relative Humidity Sensors onto Packaged Integrated Circuits. *Sensor. Actuator. B Chem.* **2018**, *255*, 1031−1038.
(16) Li, Y.; Wang, G.; Ye, K.; Cheng, K.; Pan, Y.; Yan, P.; Yin, J.; Cao, D. Facile Preparation of Three-Dimensional Multilayer Porous MnO2/reduced Graphene Oxide Composite and Its Supercapacitive Performance. *J. Power Sources* **2014**, *271*, 582−588.
(17) Lampert, C. M. Large-Area Smart Glass and Integrated Photovoltaics. *Sol. Energy Mater. Sol. Cells* **2003**, *76*, 489−499.
(18) Torrisi, F.; Hasan, T.; Wu, W.; Sun, Z.; Lombardo, A.; Kulmala, T. S.; Hsieh, G.-W.; Jung, S.; Bonaccorso, F.; Paul, P. J.; Chu, D.; Ferrari, A. C. Inkjet-Printed Graphene Electronics. *ACS Nano* **2012**, *6*, 2992−3006.
(19) Hecht, D. S.; Hu, L.; Irvin, G. Emerging Transparent Electrodes Based on Thin Films of Carbon Nanotubes, Graphene, and Metallic Nanostructures. *Adv. Mater.* **2011**, *23*, 1482−1513.
(20) Bonaccorso, F.; Sun, Z.; Hasan, T.; Ferrari, A. C. Graphene Photonics and Optoelectronics. *Nat. Photon.* **2010**, *4*, 611−622.
(21) De, S.; Coleman, J. N. The Effects of Percolation in Nanostructured Transparent Conductors. *MRS Bull.* **2011**, *36*, 774−781.
(22) Kim, Y. H.; Sachse, C.; MacHala, M. L.; May, C.; Müller-Meskamp, L.; Leo, K. Highly Conductive PEDOT: PSS Electrode with Optimized Solvent and Thermal Post-Treatment for ITO-Free Organic Solar Cells. *Adv. Funct. Mater.* **2011**, *21*, 1076−1081.
(23) Jørgensen, M.; Norrman, K.; Krebs, F. C. Stability/Degradation of Polymer Solar Cells. *Sol. Energy Mater. Sol. Cells* **2008**, *92*, 686.
(24) Yun, J.-M.; Yeo, J.-S.; Kim, J.; Jeong, H.-G.; Kim, D.-Y.; Noh, Y.-J.; Kim, S.-S.; Ku, B.-C.; Na, S.-I. Solution-Processable Reduced Graphene Oxide as a Novel Alternative to PEDOT: PSS Hole Transport Layers for Highly Efficient and Stable Polymer Solar Cells. *Adv. Mater.* **2011**, *23*, 4923−4928.
(25) McCarthy, J. E.; Hanley, C. A.; Brennan, L. J.; Lambertini, V. G.; Gun'ko, Y. K. Fabrication of Highly Transparent and Conducting PEDOT: PSS Films Using a Formic Acid Treatment. *J. Mater. Chem. C* **2014**, *2*, 764−770.
(26) Carey, T.; Cacovich, S.; Divitini, G.; Ren, J.; Mansouri, A.; Kim, J. M.; Wang, C.; Ducati, C.; Sordan, R.; Torrisi, F. Fully Inkjet-Printed Two-Dimensional Material Field-Effect Heterojunctions for Wearable and Textile Electronics. *Nat. Commun.* **2017**, *8*, 1202.
(27) Call, T. P.; Carey, T.; Bombelli, P.; Lea-Smith, D. J.; Hooper, P.; Howe, C. J.; Torrisi, F. Platinum-Free, Graphene Based Anodes and Air Cathodes for Single Chamber Microbial Fuel Cells. *J. Mater. Chem. A* **2017**, *5*, 23872−23886.
(28) Bianchi, V.; Carey, T.; Viti, L.; Li, L.; Linfield, E. H.; Davies, A. G.; Tredicucci, A.; Yoon, D.; Karagiannidis, P. G.; Lombardi, L.; Tomarchio, F.; Ferrari, A. C.; Torrisi, F.; Vitiello, M. S. Terahertz Saturable Absorbers from Liquid Phase Exfoliation of Graphite. *Nat. Commun.* **2017**, *8*, 15763.
(29) Lefebvre, A. *Atomization and Sprays*; Hemisphere Publishing Corporation, 1988.
(30) Ryntz, R. A.; Yaneff, P. V. *Coatings of Polymers and Plastics*; Marcel Dekker Inc.: New York, 2003.
(31) Lefebvre, A. H. Properties of Sprays. *Part. Part. Syst. Char.* **1989**, *6*, 176−186.
(32) Hinze, J. O. Fundamentals of the Hydrodynamic Mechanism of Splitting in Dispersion Processes. *AIChE J.* **1955**, *1*, 289−295.
(33) Anderson, W. E.; Yang, V. Fundamental Mechanisms of Combustion Instabilities: Aerodynamic Effects on Primary and Secondary Spray Breakup. *Liquid Rocket Engine Combustion Instability; Progress in Astronautics and Aeronautics*; American Institute of Aeronautics and Astronautics, 1995; pp 247−279.
(34) Rioboo, R.; Tropea, C.; Marengo, M. Outcomes from a Drop Impact on Solid Surfaces. *Atomization Sprays* **2001**, *11*, 12.
(35) Li, D.; Neumann, A. W. Equation of State for Interfacial Tensions of Solid-Liquid Systems. *Adv. Colloid Interface Sci.* **1992**, *39*, 299−345.
(36) Deegan, R. D.; Bakajin, O.; Dupont, T. F.; Huber, G.; Nagel, S. R.; Witten, T. A. Capillary Flow as the Cause of Ring Stains from Dried Liquid Drops. *Nature* **1997**, *389*, 827−829.
(37) Reale, A.; La Notte, L.; Salamandra, L.; Polino, G.; Susanna, G.; Brown, T. M.; Brunetti, F.; Di Carlo, A. Spray Coating for Polymer Solar Cells: An Up-to-Date Overview. *Energy Technol.* **2015**, *3*, 385−406.
(38) Razza, S.; Castro-Hermosa, S.; Di Carlo, A.; Brown, T. M. Research Update: Large-Area Deposition, Coating, Printing, and Processing Techniques for the Upscaling of Perovskite Solar Cell Technology. *APL Mater.* **2016**, *4*, 091508.
(39) Jung, M.-H.; Choi, H.-S. Surface Treatment of Indium Tin Oxide Using Radio Frequency Atmospheric and Low Pressure Plasma for OLEDs. *J. Electrochem. Soc.* **2008**, *155*, H334.
(40) De, S.; King, P. J.; Lyons, P. E.; Khan, U.; Coleman, J. N. Size Effects and the Problem with Percolation in Nanostructured Transparent Conductors. *ACS Nano* **2010**, *4*, 7064−7072.
(41) Funk, J. E.; Dinger, D. *Predictive Process Control of Crowded Particulate Suspensions*. Applied to Ceramic Manufacturing; Springer, 1994.
(42) Scardaci, V.; Coull, R.; Lyons, P. E.; Rickard, D.; Coleman, J. N. Spray Deposition of Highly Transparent, Low-Resistance Networks of Silver Nanowires over Large Areas. *Small* **2011**, *7*, 2621−2628.
(43) Majumder, M.; Rendall, C.; Li, M.; Behabtu, N.; Eukel, J. A.; Hauge, R. H.; Schmidt, H. K.; Pasquali, M. Insights into the Physics of Spray Coating of SWNT Films. *Chem. Eng. Sci.* **2010**, *65*, 2000−2008.
(44) Barrows, A. T.; Pearson, A. J.; Kwak, C. K.; Dunbar, A. D. F.; Buckley, A. R.; Lidzey, D. G. Efficient Planar Heterojunction Mixed-Halide Perovskite Solar Cells Deposited via Spray-Deposition. *Energy Environ. Sci.* **2014**, *7*, 2944−2950.
(45) Lotya, M.; Hernandez, Y.; King, P. J.; Smith, R. J.; Nicolosi, V.; Karlsson, L. S.; Blighe, F. M.; De, S.; Wang, Z.; McGovern, I. T.; Duesberg, G. S.; Coleman, J. N. Liquid Phase Production of Graphene by Exfoliation of Graphite in Surfactant/water Solutions. *J. Am. Chem. Soc.* **2009**, *131*, 3611−3620.
(46) Hernandez, Y.; Nicolosi, V.; Lotya, M.; Blighe, F. M.; Sun, Z.; De, S.; McGovern, I. T.; Holland, B.; Byrne, M.; Gun'Ko, Y.; Boland, J. J.; Niraj, P.; Duesberg, G.; Krishnamurthy, S.; Goodhue, R.; Hutchison, J.; Scardaci, V.; Ferrari, A. C.; Coleman, J. N. High Yield Production of Graphene by Liquid Phase Exfoliation of Graphite. *Nat. Nanotechnol.* **2008**, *3*, 563−568.
(47) Sternling, C. V.; Scriven, L. E. Interfacial Turbulence: Hydrodynamic Instability and the Marangoni Effect. *AIChE J.* **1959**, *5*, 514−523.
(48) Bernardin, J. D.; Mudawar, I. A Leidenfrost Point Model for Impinging Droplets and Sprays. *J. Heat Tran.* **2004**, *126*, 272.

DOI: 10.1021/acsami.8b02784
ACS Appl. Mater. Interfaces 2018, 10, 19948−19956

(49) Giordani, S.; Bergin, S. D.; Nicolosi, V.; Lebedkin, S.; Kappes, M. M.; Blau, W. J.; Coleman, J. N. Debundling of Single-Walled Nanotubes by Dilution: Observation of Large Populations of Individual Nanotubes in Amide Solvent Dispersions. *J. Phys. Chem. B* **2006**, *110*, 15708−15718.
(50) Chang, S. H.; Chiang, C.-H.; Kao, F.-S.; Tien, C.-L.; Wu, C.-G. Unraveling the Enhanced Electrical Conductivity of PEDOT: PSS Thin Films for ITO-Free Organic Photovoltaics. *IEEE Photonics J.* **2014**, *6*, 1.
(51) Berciaud, S.; Cognet, L.; Poulin, P.; Weisman, R. B.; Lounis, B. Absorption Spectroscopy of Individual Single-Walled Carbon Nanotubes. *Nano Lett.* **2007**, *7*, 1203−1207.
(52) Xia, X.; Wang, S.; Jia, Y.; Bian, Z.; Wu, D.; Zhang, L.; Cao, A.; Huang, C. Infrared-Transparent Polymer Solar Cells. *J. Mater. Chem.* **2010**, *20*, 8478.
(53) Okajima, H.; Kakuma, S.; Uchida, K.; Wakimoto, Y.; Noda, K. Measurement of Methane Gas Concentration Using an Infrared LED. *2006 SICE-ICASE International Joint Conference*, 2006; pp 1652−1655.
(54) Mott, N. F.; Davis, A. *Electronic Processes in Non-Crystalline Materials*; Oxford University Press: Oxford, 1971.
(55) Ferrari, A. C.; Basko, D. M. Raman Spectroscopy as a Versatile Tool for Studying the Properties of Graphene. *Nat. Nanotechnol.* **2013**, *8*, 235−246.
(56) Ferrari, A. C.; Meyer, J. C.; Scardaci, V.; Casiraghi, C.; Lazzeri, M.; Mauri, F.; Piscanec, S.; Jiang, D.; Novoselov, K. S.; Roth, S.; Geim, A. K. Raman Spectrum of Graphene and Graphene Layers. *Phys. Rev. Lett.* **2006**, *97*, 187401.
(57) Ferrari, A. C.; Robertson, J. Interpretation of Raman Spectra of Disordered and Amorphous Carbon. *Phys. Rev. B: Condens. Matter Mater. Phys.* **2000**, *61*, 14095−14107.
(58) Torrisi, F.; Hasan, T.; Wu, W.; Sun, Z.; Lombardo, A.; Kulmala, T. S.; Hsieh, G.-W.; Jung, S.; Bonaccorso, F.; Paul, P. J.; Chu, D.; Ferrari, A. C. Inkjet-Printed Graphene Electronics. *ACS Nano* **2012**, *6*, 2992−3006.
(59) Casiraghi, C.; Hartschuh, A.; Qian, H.; Piscanec, S.; Georgi, C.; Fasoli, A.; Novoselov, K. S.; Basko, D. M.; Ferrari, A. C. Raman Spectroscopy of Graphene Edges. *Nano Lett.* **2009**, *9*, 1433−1441.
(60) Dresselhaus, M. S.; Dresselhaus, G.; Saito, R.; Jorio, A. Raman Spectroscopy of Carbon Nanotubes. *Phys. Rep.* **2005**, *409*, 47−99.
(61) Garreau, S.; Louarn, G.; Buisson, J. P.; Froyer, G.; Lefrant, S. In Situ Spectroelectrochemical Raman Studies of poly(3,4-Ethylenedioxythiophene) (PEDT). *Macromolecules* **1999**, *32*, 6807−6812.
(62) Farah, A. A.; Rutledge, S. A.; Schaarschmidt, A.; Lai, R.; Freedman, J. P.; Helmy, A. S. Conductivity Enhancement of poly(3,4-Ethylenedioxythiophene)-Poly(styrenesulfonate) Films Post-Spincasting. *J. Appl. Phys.* **2012**, *112*, 113709.
(63) Zhu, B.; Niu, Z.; Wang, H.; Leow, W. R.; Wang, H.; Li, Y.; Zheng, L.; Wei, J.; Huo, F.; Chen, X. Microstructured Graphene Arrays for Highly Sensitive Flexible Tactile Sensors. *Small* **2014**, *10*, 3625−3631.
(64) Böhmer, M. *Beginning Android ADK with Arduino*. Technology in action series; Apress, 2012; p 298.
(65) Bae, S.; Kim, S. J.; Shin, D.; Ahn, J.-H.; Hong, B. H. Towards Industrial Applications of Graphene Electrodes. *Phys. Scr.* **2012**, *T146*, 014024.
(66) Cotton, D. P. J.; Graz, I. M.; Lacour, S. P. A Multifunctional Capacitive Sensor for Stretchable Electronic Skins. *IEEE Sens. J.* **2009**, *9*, 2008−2009.
(67) Yao, S.; Zhu, Y. Wearable Multifunctional Sensors Using Printed Stretchable Conductors Made of Silver Nanowires. *Nanoscale* **2014**, *6*, 2345.
(68) Hayashi, Y.; Miura, N.; Shinyashiki, N.; Yagihara, S. Free Water Content and Monitoring of Healing Processes of Skin Burns Studied by Microwave Dielectric Spectroscopy in Vivo. *Phys. Med. Biol.* **2005**, *50*, 599−612.
(69) Jo, K.; Lee, T.; Choi, H. J.; Park, J. H.; Lee, D. J.; Lee, D. W.; Kim, B.-S. Stable Aqueous Dispersion of Reduced Graphene Nanosheets via Non-Covalent Functionalization with Conducting Polymers and Application in Transparent Electrodes. *Langmuir* **2011**, *27*, 2014−2018.

DOI: 10.1021/acsami.8b02784
ACS Appl. Mater. Interfaces 2018, 10, 19948−19956